Nanoscale

RSC Publishing

PAPER

View Article Online
View Journal | View Issue

Cite this: *Nanoscale*, 2013, **5**, 5561

Controlled 3D-coating of the pores of highly ordered mesoporous antiferromagnetic Co_3O_4 replicas with ferrimagnetic $Fe_xCo_{3-x}O_4$ nanolayers†

Eva Pellicer,*[a] Moisés Cabo,[a] Alberto López-Ortega,[b] Marta Estrader,*[bc] Lluís Yedra,[de] Sònia Estradé,[de] Francesca Peiró,[e] Zineb Saghi,[f] Paul Midgley,[f] Emma Rossinyol,[g] Igor V. Golosovsky,[h] Alvaro Mayoral,[i] Joan D. Prades,[j] Santiago Suriñach,[a] Maria Dolors Baró,[a] Jordi Sort[k] and Josep Nogués[l]

Received 25th February 2013
Accepted 9th April 2013

DOI: 10.1039/c3nr00989k

www.rsc.org/nanoscale

The controlled filling of the pores of highly ordered mesoporous antiferromagnetic Co_3O_4 replicas with ferrimagnetic $Fe_xCo_{3-x}O_4$ nanolayers is presented as a proof-of-concept toward the integration of nanosized units in highly ordered, heterostructured 3D architectures. Antiferromagnetic (AFM) Co_3O_4 mesostructures are obtained as negative replicas of KIT-6 silica templates, which are subsequently coated with ferrimagnetic (FiM) $Fe_xCo_{3-x}O_4$ nanolayers. The tuneable magnetic properties, with a large exchange bias and coercivity, arising from the FiM/AFM interface coupling, confirm the microstructure of this novel two-phase core–shell mesoporous material. The present work demonstrates that ordered functional mesoporous 3D-materials can be successfully infiltrated with other compounds exhibiting additional functionalities yielding highly tuneable, versatile, non-siliceous based nanocomposites.

Introduction

Nanoscale heterostructured materials are opening new avenues for many applications due to the synergetic combination of the functional properties of their individual constituents.[1–3] The assembling of different inorganic components by chemical procedures in 1D and 2D structures has already been established.[4–8] Mesoporous siliceous materials have been demonstrated to be very versatile as platforms to attach a great variety of molecules and/or as hosts to accommodate diverse compounds within their channels,[9–12] making them suitable for applications including photonics,[13] biomedicine[14] or heterogeneous catalysis.[15] This has led to a new generation of silica-based smart hybrid nanomaterials with fascinating morphologies. However, owing to its rather chemical inertness and its limited degree of additional functional properties, silica is mainly a *passive component* in these hybrid structures (bringing only large surface areas) and its main functionalities arise from the guest compound. To increase the functionality of mesoporous materials, significant progress has been made toward the fabrication of non-siliceous replicas with different symmetries, maintaining large surface areas, through hard-template methods.[16] Compared to silica, transition metal oxides can be considered as *chemically active* and have a rich variety of *practical physicochemical properties*, thus significantly broadening the applicability of mesoporous materials to numerous novel fields.[17] Yet, successful mesoporous replication is rather challenging and largely depends on the synthesis conditions. Thus, it is often accompanied by a loss of mesostructural order, which

[a]*Departament de Física, Facultat de Ciències, Universitat Autònoma de Barcelona, E-08193 Bellaterra, Spain. E-mail: eva.pellicer@uab.cat*

[b]*CIN2(ICN-CSIC) and Universitat Autònoma de Barcelona, Catalan Institute of Nanotechnology, Campus de la UAB, E-08193 Bellaterra, Spain. E-mail: martaestrader@gmail.com*

[c]*Departament de Química Inorgànica, Universitat de Barcelona, Diagonal 647, 08028, Barcelona, Spain*

[d]*TEM-MAT, CCiT-Universitat de Barcelona, Solé i Sabaris 1, E-08028, Barcelona, Spain*

[e]*LENS-MIND-IN^{2}UB, Departament d'Electrònica, Universitat de Barcelona, Martí i Franquès 1, E-08028 Barcelona, Spain*

[f]*Department of Materials Science and Metallurgy, University of Cambridge, Pembroke Street, Cambridge CB2 3QZ, UK*

[g]*Servei de Microscòpia, Universitat Autònoma de Barcelona, E-08193 Bellaterra, Spain*

[h]*Petersburg Nuclear Physics Institute, Gatchina, 188300, St. Petersburg, Russia*

[i]*Laboratorio de Microscopías Avanzadas (LMA), Instituto de Nanociencia de Aragón (INA), Universidad de Zaragoza, Mariano Esquillor s/n, 50018, Zaragoza, Spain*

[j]*EME/XaRMAE/IN^{2}UB, Departament d'Electrònica, Universitat de Barcelona and Institut de Recerca en Energia de Catalunya (IREC), Spain*

[k]*Institució Catalana de Recerca i Estudis Avançats (ICREA) and Departament de Física, Universitat Autònoma de Barcelona, E-08193 Bellaterra, Spain*

[l]*Institució Catalana de Recerca i Estudis Avançats (ICREA) and CIN2(ICN-CSIC) and Universitat Autònoma de Barcelona, Catalan Institute of Nanotechnology, Campus de la UAB, E-08193 Bellaterra, Spain*

† Electronic supplementary information (ESI) available: FESEM image of KIT-6 mesoporous particles corresponding to the Co_3O_4 template and Co_3O_4–Fe4 sample. EELS analysis of Co_3O_4–Fe1 and Co_3O_4–Fe4 samples. X-ray diffraction pattern of the Co_3O_4–Fe6 sample and neutron diffraction pattern of the Co_3O_4 mesoporous template. Videos of Co_3O_4 and Co_3O_4–Fe4 particles. See DOI: 10.1039/c3nr00989k

precludes their use as a second template to be potentially filled with another material. Consequently, the choice of an appropriate system is the first issue for obtaining a high-quality replica that could be thereafter employed as a host. Filling a high-quality active template with a second material featuring a different practical property would render a multifunctional nanocomposite, not only by the addition of the diverse properties of the counterparts, but also due to their mutual interactions. Interestingly, such mesostructures would be able to perform more than one task at a time or allow the control of one of the components due to the presence of the other.

Here we establish the feasibility to synthesize highly ordered 3D heterostructured nanocomposite structures by coating the walls of antiferromagnetic (AFM) Co_3O_4 mesoporous replicas with a ferrimagnetic (FiM) $Fe_xCo_{3-x}O_4$ layer. The magnetic performance of the core–shell nanocomposites is shown to arise from the combination of the individual properties. Remarkably, we demonstrate that the exchange interaction between the AFM and FiM constituents can be used for the *post-synthesis* tuning of the magnetic properties.

Results and discussion

Shown in Fig. 1 is a schematic picture of the pathway followed for the synthesis of the $Fe_xCo_{3-x}O_4$@Co_3O_4 nanocomposites. Steps 1–3 comprise the synthesis of the KIT-6 silica template and Co_3O_4 as its negative replica. The Co_3O_4 KIT-6 replica is subsequently infiltrated with variable amounts of iron nitrate (step 4) followed by calcination (step 5). The resulting heterostructured powders are denoted as Co_3O_4–Fe1, Co_3O_4–Fe2, Co_3O_4–Fe4 and Co_3O_4–Fe6, according to the increased loading.

The scanning electron microscopy image of the mesoporous Co_3O_4 replica reveals rather dense spheres, featuring a regular porous periodicity at the surface level (Fig. 2(a)). Actually, two coupled frameworks constitute the morphology of the material, as expected from the KIT-6 structure (*Ia3d* symmetry), constructed by two enantiomeric sets of channel networks forming a bicontinuous structure.[18] The typical hexagonal KIT-6 rings are clearly visible in the transmission electron microscopy image (Fig. 2(b), top inset). The pore diameter is around 11 nm and the wall thickness is about 5 nm (Fig. 2(b)), correlating with the parent template. The well-defined spots in the selected area electron diffraction prove the high crystallinity of the Co_3O_4 walls (Fig. 2(b), bottom inset). Importantly, the 3-dimensional structure of pores is impressively revealed by the 3D tomographic reconstruction (see ESI Videos†).

As the Fe(III) : Co_3O_4 ratio increases, the spheres appear progressively denser, with a *less open* pore structure (ESI, Fig. S1†). Analysis of the apparent skeleton thickness confirms the progressive impregnation of the 3D Co_3O_4 host and evidences the structural integrity of the loaded samples (Fig. 2(c) and (d)). The mesopore wall thickness increases from 5.1 nm in pure Co_3O_4 to 7.8 nm for Co_3O_4–Fe4. This suggests that the iron-based material covers the Co_3O_4 skeleton, forming a shell around the Co_3O_4 pore walls. This is clearly evidenced by the electron energy loss spectra (EELS) mapping of Co_3O_4–Fe2 (Fig. 2(e) and (f)), where the green colour (Co) predominates in

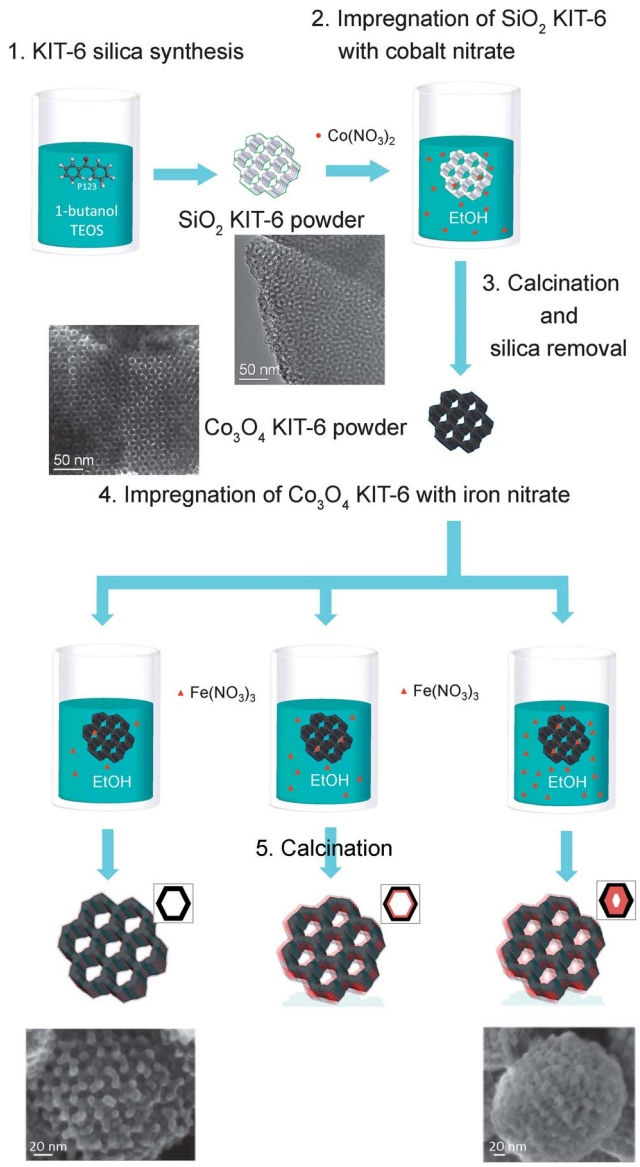

Fig. 1 Schematic illustration of the synthesis pathway. *Step 1*: preparation of KIT-6 silica by using Pluronic P123 as the surfactant and tetraethoxysilane (TEOS) as the silicon source. A transmission electron microscope (TEM) image of the KIT-6 silica template is shown. *Step 2*: impregnation of KIT-6 silica with cobalt nitrate in ethanol media. *Step 3*: calcination to convert the cobalt nitrate salt into the oxide, followed by silica removal to release the Co_3O_4 replica. A TEM image of Co_3O_4 KIT-6 is shown. *Step 4*: impregnation of mesoporous Co_3O_4 with increasingly high amounts of iron nitrate in ethanol media. *Step 5*: calcination of the impregnated Co_3O_4 materials to obtain the final nanocomposites. Shown in red is the progressively thicker iron-based layer coating the Co_3O_4 walls. Field emission scanning electron microscope (FESEM) images of the $Fe_xCo_{3-x}O_4$@Co_3O_4 nanocomposite with different Fe loading levels are shown.

the skeleton of the Co_3O_4 matrix, whilst the red pixels (Fe) are located in the vicinity of the pore edges. In concordance with the pore thickness analysis, the EELS mapping of Co_3O_4–Fe1 (with less iron) shows a much thinner Fe-based wall around the pores (ESI, Fig. S2†). Remarkably, the 3D-structure of the filled pores is distinctly established by the 3D tomographic reconstruction of Co_3O_4–Fe4, where a 3D arrangement of narrow pores can be identified (ESI Video†). Closer inspection of

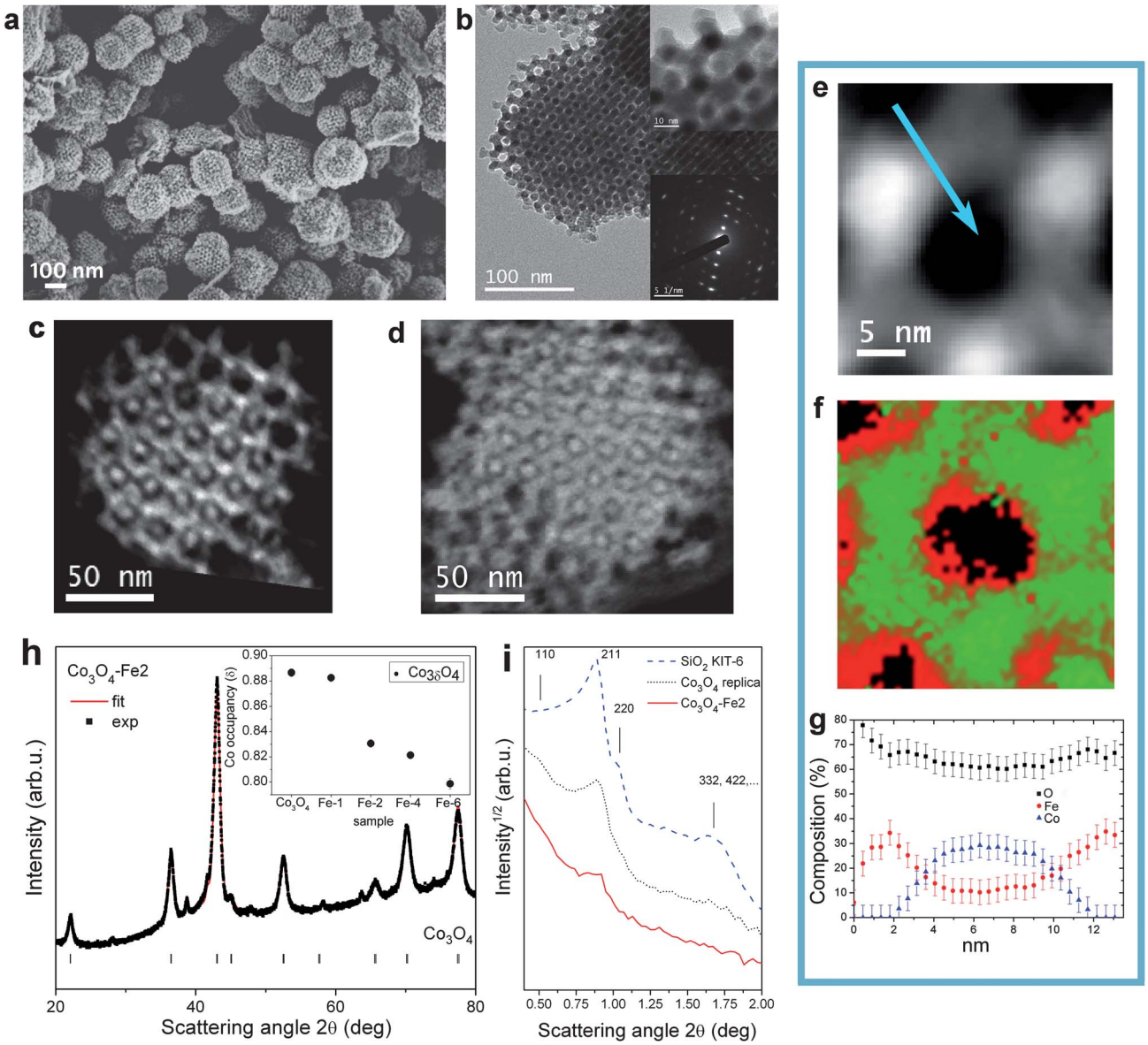

Fig. 2 Morphological, compositional and structural characterization. (a) FESEM image of non-infiltrated mesoporous Co_3O_4 powder. (b) TEM image of a single Co_3O_4 particle (top: enlarged view of the hexagonal rings, bottom: selected area electron diffraction (SAED) pattern). Slices through the tomographic 3D reconstruction of (c), non-infiltrated Co_3O_4 and (d), Co_3O_4–Fe4 particles. (e) TEM image of a pore of the Co_3O_4–Fe2 particle. (f) EELS map of (e) [Co – bright green, Fe – bright red]. (g) EELS relative elemental quantification along the line indicated in (e). (h) Experimental wide-angle pattern and Rietveld-fit of the Co_3O_4–Fe2 sample. Shown at the bottom are the peak positions for Co_3O_4. The inset shows the cobalt occupancy (δ) for different samples. (i) Low-angle patterns of the KIT-6 SiO_2 parent template, Co_3O_4 and Co_3O_4–Fe2 samples.

Fig. 2(f) seems to indicate a graded Co–Fe composition around the pore edges. Indeed, the EELS relative elemental quantification across the pore wall (Fig. 2(g)) evidences the formation of a graded nanolayer. In fact, a 2 nm thick pure Fe_3O_4–Fe_2O_3 layer can be clearly identified away from the replica walls. This is followed by a $Fe_xCo_{3-x}O_4$ (with $x \sim 3.0$ to 0.7) gradient towards the center of the replica walls. This indicates that apart from the formation of a thin Fe_3O_4–Fe_2O_3 layer, some of the Fe ions have diffused into the Co_3O_4 walls (although some contribution from Fe-oxide grown *on top* of the wall cannot be ruled out). Similar results are also observed in the Co_3O_4–Fe1 and Co_3O_4–Fe4 powders (ESI, Fig. S2, S3 and Table S1†). Interestingly, it has been recently reported that for lower Fe(III):Co_3O_4 molar ratios (0.48) virtually all the Fe species diffuse into the Co_3O_4 matrix leading to a Fe-doped Co_3O_4 mesoporous material, without any apparent increase in the wall thickness.[19] In contrast, the EELS mapping of the present $Fe_xCo_{3-x}O_4$@Co_3O_4 nanocomposites (obtained with higher Fe(III) : Co_3O_4 molar ratios) unambiguously demonstrates the formation of a core–shell structure.

Significantly, unstructured particles are not observed, except for Co_3O_4–Fe6, which also shows iron oxide (α-Fe_2O_3) non-mesoporous particles (revealed by energy-dispersive X-ray spectroscopy and X-ray diffraction (XRD) analyses; see ESI, Fig. S4†) outside the Co_3O_4 host. Hence, the maximum loading

of the Co_3O_4 matrix allowing to maximize the amount of embedded $Fe_xCo_{3-x}O_4$ while avoiding the growth of the material outside the mesoporous structure corresponds to a Fe(III) : Co_3O_4 = 2.4 molar ratio. The wide-angle XRD patterns of the $Fe_xCo_{3-x}O_4$@Co_3O_4 composites and the corresponding Rietveld fits[20] confirm the presence of the spinel-type Co_3O_4 phase (Fig. 2(h)) with an averaged correlation length ~9 nm (independent of the loading). However, the Co occupancy diminishes (Fig. 2(h), inset) and the lattice parameter increases with the loading indicating the incorporation of Fe ions into the Co_3O_4 lattice and the concomitant exchange between Fe and Co ions. Note that even for Co_3O_4–Fe2 some minor peaks corresponding to α-Fe_2O_3 can also be identified. From the peak width it can be concluded that the α-Fe_2O_3 phase is exceedingly large (~20 nm) to be inside the pores. Consequently these peaks must correspond also to a tiny fraction of α-Fe_2O_3 nanoparticles outside the mesoporous structure. Nevertheless, its amount is very low (around 2 wt%).

The low-angle XRD curve of the parent KIT-6 SiO_2 template shows the characteristic reflections of a gyroidal mesostructure[18,21] (Fig. 2(i)). The (211), (220) and (332) reflections, though less intense, are still observed in the Co_3O_4 replica. From the (211) reflection the mesostructural unit-cell parameter of Co_3O_4 was evaluated as 23.0 (5) nm. The extinction of the (110) reflection is indicative of the dominance of undisplaced double gyroidal frameworks. Due to the formation of $Fe_xCo_{3-x}O_4$ onto the Co_3O_4 pore walls the low-angle curves of the nanocomposites became progressively less well-defined, although the presence of the (211) peak certifies the preservation of the long-range order even in the loaded samples.[22]

The pure Co_3O_4 magnetization *vs.* field, $M(H)$, curve exhibits a linear behaviour (Fig. 3(a)), while the temperature dependence of the magnetization, $M(T)$, shows a maximum at $T = 30$ K with only a weak dependence on the field cooling/zero field cooling (FC/ZFC) conditions (Fig. 3(b), inset). This indicates that the mesoporous Co_3O_4 behaves like an antiferromagnet with a Néel temperature, $T_N \sim 30$ K (as also demonstrated by neutron diffraction, see ESI, Fig. S5†), in concordance with bulk Co_3O_4[23] and other studies on mesoporous Co_3O_4,[24–26] although more detailed investigations reveal more complex behaviour.[27] The hysteresis loop for Co_3O_4–Fe2 exhibits a clear ferromagnetic nature (Fig. 3(a)), with a saturation magnetization of $M_S = 5.6$ emu g^{-1} and a large coercivity, $H_C = 8730$ Oe. This behaviour must be ascribed to the presence of $Fe_xCo_{3-x}O_4$, which is FiM.[28,29] In fact, given the compositional gradient and the relatively low magnetic anisotropy of Fe_3O_4–Fe_2O_3 and the large anisotropy of $CoFe_2O_3$, the magnetism of the nanolayer can be thought of as a gradient anisotropy material, similar to thin films or core–shell nanoparticles[30,31] probably leading to the broad maxima observed in the $M(T)$ ZFC curves (Fig. 3(b), inset). Namely, due to the small dimensions involved the magnetically soft and hard counterparts are strongly exchange coupled leading to smooth hysteresis loops with averaged properties.[32] Co_3O_4–Fe1 presents a similar behaviour although with a smaller M_S, $M_S = 3.7$ emu g^{-1}, indicating a lesser amount of $Fe_xCo_{3-x}O_4$, as expected from the synthesis and demonstrated by the EELS mapping. The FC/ZFC $M(T)$ curves for both samples

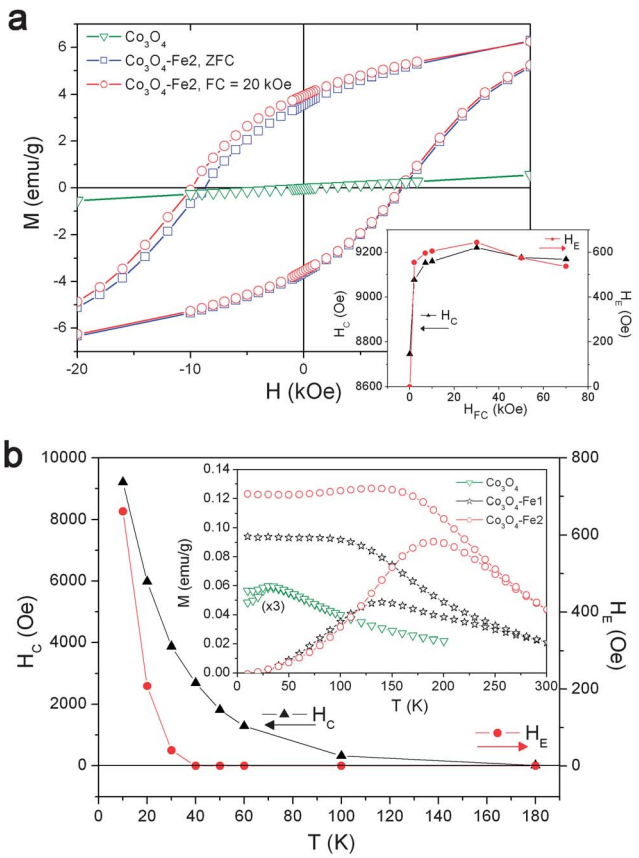

Fig. 3 Magnetic properties. (a) Magnetization *vs.* field curves, $M(H)$, at 10 K for pure Co_3O_4 and Co_3O_4–Fe2 samples after cooling them at room temperature either in zero field (ZFC) or applying a magnetic field of 20 kOe (FC). The inset shows the dependence of H_C and H_E at 10 K on the magnetic field applied during the cooling procedure (H_{FC}) for the Co_3O_4–Fe2 sample. (b) Temperature dependence of H_C and H_E after field cooling with $H_{FC} = 20$ kOe for the Co_3O_4–Fe2 sample The inset shows the ZFC/FC $M(T)$ curves of the different samples recorded applying a magnetic field of 20 Oe.

display a behaviour typical for interacting superparamagnetic (SP) nanostructures (Fig. 3(b), inset), where M_{ZFC} shows a maximum at the SP–FiM transition (*i.e.*, blocking temperature, T_B).[33] However, T_B for Co_3O_4–Fe1 is lower than that for Co_3O_4–Fe2. Since $T_B = KV/25k_B$,[33] (where K, V and k_B are the anisotropy, the volume and the Boltzmann constant), the raise in T_B for Co_3O_4–Fe2 is in line with the FiM volume increase.

For Co_3O_4–Fe2, the hysteresis loop after field cooling exhibits a loop shift in the field axis, $H_E = 660$ Oe, and an enhanced H_C, $H_C = 9200$ Oe (Fig. 3(a)). These are well known effects of FiM/AFM exchange coupling and have been observed in different types of morphologies, *e.g.*, thin films,[34] core–shell nanoparticles[35] or FM nanoparticles embedded in AFM matrices.[36] However, note that the morphology of the present samples renders a 3D-ordered FM/AFM structure in contrast to most of the systems involving nanoparticles or 3D structures which exhibit a random distribution.[24,37–39] Moreover, given the inverse dependence of H_E on the FiM thickness[35] and the morphology of the samples, with thin FiM coatings on the walls of the Co_3O_4 AFM matrix, H_E is considerably larger than the one observed for Co_3O_4 based thin films.[40] Nevertheless, Fe-doped Co_3O_4 mesoporous materials

also exhibit large H_C and H_E values.[19] The temperature dependence of H_C and H_E (Fig. 3(b)) shows that while H_E vanishes at $T = 40$ K (*i.e.*, around T_N of Co_3O_4), H_C remains finite until 180 K. This unambiguously demonstrates the intimate contact between the Co_3O_4 template and the infiltrated FiM material, which results in a dramatic change of the magnetic properties. These materials also reveal an interesting FC dependence of the FiM magnetic properties. Namely, H_C, H_E (see Fig. 3(a), inset) and the remanent magnetization, M_R (*i.e.*, magnetization at zero field), can be controlled by the cooling field, similar to thin film and core–shell systems.[35,41–43] Namely, for small H_{FC} the FiM is not fully saturated thus the FiM/AFM coupling is not optimized leading to a small H_E and H_C. As H_{FC} increases, all the FiM are aligned with H_{FC} during the cooling procedure, leading to the maximum values of H_E and H_C. Thus, the AFM character of the Co_3O_4 template influences the response of the FiM phase, allowing for a tailoring of the magnetic properties of the overall heterostructure.

Conclusions

Summarizing, we demonstrate that the mesopore walls of a KIT-6 Co_3O_4 material can be effectively and controllably coated by a nanolayer of a ferrimagnetic material through an *all-chemical procedure*. Due to the inherited pore periodicity of the $Fe_xCo_{3-x}O_4$ nanocasting, the resulting heterostructure maintains a large degree of porosity. The 3D-ordered nanocomposite is shown to have tuneable magnetic properties controlled not only by the relative amount of each component but also by their mutual interactions. Importantly, this approach might be extrapolated to other types of materials with numerous different combinations of functionalities (*e.g.*, catalytic, magnetic, electrical or optical). Thus, the versatility, simplicity and cost-effectiveness in the synthesis of these heterostructured materials will open new opportunities for the controlled integration of different inorganic compounds in an ordered, multifunctional 3D core–shell architecture, which may further expand the use of two-phase mesoporous materials in very diverse fields like adsorption, separation, drug-delivery, fuel-cells, sensors, MRI-imaging, hyperthermia or even magnetic recording.

Methods

Synthesis of the mesoporous samples

Mesoporous KIT-6 silica was synthesized by dissolving 6.0 g of Pluronic P123 copolymer (from BASF) in diluted HCl in a plastic bottle. Once the P123 surfactant completely dissolved, 6.0 g of 1-butanol were added and the solution was stirred for 1 h. 12.5 g of tetraethyl orthosilicate (TEOS) were added to the solution and further stirred for 24 h at a constant temperature (34–35 °C). The hydrothermal treatment of the milky suspension was carried out at 90 °C for 24 h in a sealed container and the solid obtained was filtered, copiously washed with water and finally calcined at 550 °C for 5 h to remove the organics.

For the synthesis of the Co_3O_4 replica, 0.150 g of KIT-6 silica was put in contact with 0.291 g of $Co(NO_3)_2 \cdot 6H_2O$ (99.9% purity) dissolved in ethanol. The mixture was stirred for 30 min in a crucible and left for ethanol evaporation overnight. The crucible was then placed in a tubular furnace and the impregnated silica was calcined under atmospheric conditions. The furnace temperature was increased to 375 °C at a rate of 3 °C min^{-1} and held at this temperature for 4 h under atmospheric conditions. At the end of this process, the furnace was slowly cooled down to room temperature. The silica host was removed with 30 mL of 2 M NaOH solution at 70 °C under stirring. The resulting mesoporous Co_3O_4 powder was collected after centrifugation and the supernatant was decanted, copiously rinsed in ethanol, and finally dried.

The Co_3O_4 KIT-6 replica was subsequently loaded with variable amounts of $Fe(NO_3)_3 \cdot 9H_2O$ (99.9% purity). Typically, 6 mg of Co_3O_4 powder was dispersed in ethanol and put in contact with the iron nitrate salt in the following Fe(III) : Co_3O_4 molar ratios: 0.6, 1.2, 2.4, and 3.6. The suspensions were gently stirred for 30 min in a crucible and left again for ethanol evaporation overnight. The impregnated Co_3O_4 powders were heated up at a rate of 1 °C min^{-1} and held at 375 °C for 4 h to allow the conversion of the iron salt into the oxide product. The filled Co_3O_4 hosts have been denoted as Co_3O_4–Fe1, Co_3O_4–Fe2, Co_3O_4–Fe4 and Co_3O_4–Fe6, respectively, according to the increased loading of the iron precursor.

Details of the characterization methods

The morphology and chemical composition of the materials were investigated by field emission scanning electron microscopy (FESEM) and transmission electron microscopy (TEM). FESEM characterization was performed on a Merlin Zeiss microscope operated at 2 kV. The powders were spread onto a silicon substrate and directly imaged under the electron beam without using any conducting surface coating. TEM characterization was carried out on Jeol-JEM 2011 equipment operated at 200 kV. Electron Energy Loss Spectra (EELS) characterization was carried out on a Jeol-JEM 2010F at 200 kV coupled with a Gatan Image Filter (GIF). Tomography experiments were performed on a FEI Tecnai F20-G2 TEM also operated at 200 kV. Aberration corrected (Cs) STEM data coupled with EELS spectrum imaging was performed on a X-FEG FEI TITAN operated at 300 kV fitted with a CEOS Probe Corrector and a Gatan Tridiem Energy Filter. For relative compositional map construction, the background was substracted using the powder law fit method and the relative composition was calculated using the Hartree–Slater-cross-section model. The pixel time was set to 0.07 s per pixel and a collection angle β of 55 mrad. Samples were prepared by dispersing a small amount of the powder in ethanol and then one or two drops of the suspension were placed dropwise onto a holey carbon supported grid. High angle annular dark field (HAADF) images for tomography were acquired every 2° in tilt series which ranged at least from −64° to 64°. The tilt series were aligned and subsequently reconstructed using 40 iterations of SIRT algorithm using Inspect3D. Visualization of the reconstruction was achieved using the Amira software.

Low-angle X-ray diffraction (XRD) patterns were recorded on a Panalytical X'Pert Pro diffractometer operating in transmission mode with Cu Kα radiation. Wide-angle XRD patterns

were collected on a Philips X'Pert diffractometer in the 20–80° 2θ range (step size = 0.03°, step time = 10 s) using Cu Kα radiation, at a voltage of 50 kV and 40 mA of current. The structural parameters were evaluated by fitting the full XRD patterns using the Fullprof program.[20]

The magnetic properties were evaluated on tightly packed powdered samples using a superconducting quantum interference device (SQUID, Quantum Design) magnetometer with a 70 kOe maximum field. The temperature dependence of the magnetization, $M(T)$, for samples Co_3O_4–Fe1 and Co_3O_4–Fe2 was measured at 20 Oe for increasing temperatures after either zero field cooling (ZFC) or field cooling (FC) in the 20 Oe from 300 K. For pure Co_3O_4, ZFC/FC $M(T)$ was obtained using 500 Oe. Hysteresis loops were carried out (i) at 10 K after FC from 300 K using different cooling magnetic field values, $H_{FC} = 2$, 7, 10, 30, 50 and 70 kOe and (ii) at different increasing values of temperatures after FC in $H_{FC} = 20$ kOe from 300 K to 10 K. Note that the magnetizations are given per total mass.

Neutron diffraction measurements were carried out at 300 K and 10 K (*i.e.*, below $T_N(Co_3O_4) = 30$ K) at the diffractometer D1B of the Institute Laue-Langevin with a neutron wavelength of 2.4 Å.

Acknowledgements

The authors sincerely thank BASF Corporation for kindly supplying the P123 precursor used in the synthesis of KIT-6 silica. This work is supported by the 2009-SGR-1292 and CTP2009-00018 projects of the Generalitat de Catalunya, the MAT2010-20616-C02, MAT2011-27380-C02-01, MAT2011-16407 and CSD2009-0013 projects of the Spanish Ministry of Economy and Competitiveness (MINECO) and the ONDA (no. FP7-PEOPLE-2009-IRSES-247518) and ESTEEM2 (312483, Integrated Infraestructure Initiative-I3, FP7) projects of the European Union. We also acknowledge SpINS and the Institute Laue-Langevin for the provision of neutron beam time and O. Fabelo for his help during the neutron diffraction measurements. I.V.G. thanks the Generalitat de Catalunya for his sabbatical fellowship (2010 PIV 00096) and the Russian grants RFBR-13-02-00121 and MESRF-16.518.11.7034. M.E. acknowledges the Spanish Ministry of Science and Innovation through the Juan de la Cierva Program. M.D.B. was partially supported by an ICREA Academia award.

Notes and references

1 S. C. Warren, L. C. Messina, L. S. Slaughter, M. Kamperman, Q. Zhou, S. M. Gruner, F. J. DiSalvo and U. Wiesner, *Science*, 2008, **320**, 1748–1752.
2 R. T. Olsson, M. A. S. Azizi Samir, G. Salazar-Alvarez, L. Belova, V. Ström, L. A. Berglund, O. Ikkala, J. Nogués and U. W. Gedde, *Nat. Nanotechnol.*, 2010, **5**, 584–588.
3 Y. Liang, Y. Li, H. Wang, J. Zhou, J. Wang, T. Regier and H. Dai, *Nat. Mater.*, 2011, **10**, 780–786.
4 J. E. Macdonald, M. Bar Sadan, L. Houben, I. Popov and U. Banin, *Nat. Mater.*, 2010, **9**, 810–815.
5 W. Gao, K. Manian Manesh, J. Hua, S. Sattayasamitsathit and J. Wang, *Small*, 2011, **7**, 2047–2051.
6 K.-Y. Chun, Y. Oh, J. Rho, J.-H. Ahn, Y.-J. Kim, H. R. Choi and S. Baik, *Nat. Nanotechnol.*, 2010, **5**, 853–857.
7 M. Gich, Ll. Casas, A. Roig, E. Molins, J. Sort, S. Suriñach, M. D. Baró, J. S. Muñoz, L. Morellon, M. R. Ibarra and J. Nogués, *Appl. Phys. Lett.*, 2003, **82**, 4307–4309.
8 M. Liu, J. Lou, S. Li and N. X. Sun, *Adv. Funct. Mater.*, 2011, **21**, 2593–2598.
9 N. K. Mal, M. Fujiwara and Y. Tanaka, *Nature*, 2003, **421**, 350–353.
10 B. González, M. Colilla, C. L. de Laorden and M. Vallet-Regí, *J. Mater. Chem.*, 2009, **19**, 9012–9024.
11 S. Zheng, F. Fang, G. Zhou, G. Chen, L. Ouyang, M. Zhu and D. Sun, *Chem. Mater.*, 2008, **20**, 3954–3958.
12 A. F. Gross, M. R. Diehl, K. C. Beverly, E. K. Richman and S. H. Tolbert, *J. Phys. Chem. B*, 2003, **107**, 5475–5482.
13 K. E. Shopsowitz, H. Qi, W. Y. Hamad and M. J. MacLachlan, *Nature*, 2010, **468**, 422–425.
14 J. L. Vivero-Escoto, I. I. Slowing, B. G. Trewyn and V. S.-Y. Lin, *Small*, 2010, **6**, 1952–1967.
15 E. Kockrick, F. Schmidt, K. Gedrich, M. Rose, T. A. George, T. Freudenberg, R. Kraehnert, R. Skomski, D. J. Sellmyer and S. Kaskel, *Chem. Mater.*, 2010, **22**, 1624–1632.
16 M. Tiemann, *Chem. Mater.*, 2008, **20**, 961–971.
17 A. H. Lu, D. Zhao and Y. Wan, *Nanocasting: A versatile strategy for creating nanostructured porous materials*, RSC Publishing, Cambridge, UK, 2010.
18 F. Kleitz, F. H. Choi and R. Ryoo, *Chem. Commun.*, 2003, 2136–2137.
19 H. Tüysüz, E. L. Salabaş, E. Bill, H. Bongard, B. Spliethoff, C. W. Lehmann and F. Schüth, *Chem. Mater.*, 2012, **24**, 2493–2500.
20 J. Rodríguez-Carvajal, *Phys. B*, 1993, **192**, 55–69.
21 L. A. Solovyov, V. I. Zaikovskii, A. N. Shmakov, O. V. Belousov and R. Ryoo, *J. Phys. Chem. B*, 2002, **106**, 12198–12202.
22 B. Tian, X. Liu, L. A. Solovyov, Z. Liu, H. Yang, Z. Zhang, S. Xie, F. Zhang, B. Tu, C. Yu, O. Terasaki and D. Zhao, *J. Am. Chem. Soc.*, 2004, **126**, 865–875.
23 W. L. Roth, *J. Phys. Chem. Solids*, 1964, **25**, 1–10.
24 M. Cabo, E. Pellicer, E. Rossinyol, M. Estrader, A. López-Ortega, J. Nogués, O. Castell, S. Suriñach and M. D. Baró, *J. Mater. Chem.*, 2010, **20**, 7021–7028.
25 Y. Wang, C.-M. Yang, W. Schmidt, B. Spliethoff, E. Bill and F. Schüth, *Adv. Mater.*, 2005, **17**, 53–56.
26 G. Wang, H. Liu, J. Horvat, B. Wang, S. Qiao, J. Park and H. Ahn, *Chem.–Eur. J.*, 2010, **16**, 11020–11027.
27 M. J. Benitez, O. Petracic, H. Tüysüz, F. Schüth and H. Zabel, *Europhys. Lett.*, 2009, **88**, 27004.
28 M. Takahashi and M. E. Fine, *J. Appl. Phys.*, 1972, **43**, 4205–4216.
29 T. E. Quickel, V. H. Le, T. Brezesinski and S. H. Tolbert, *Nano Lett.*, 2010, **10**, 2982–2988.
30 C. L. Zha, R. K. Dumas, Y. Y. Fang, V. Bonanni, J. Nogués and J. Åkerman, *Appl. Phys. Lett.*, 2010, **97**, 182504.
31 A. López-Ortega, M. Estrader, G. Salazar-Alvarez, S. Estradé, I. V. Golosovsky, R. K. Dumas, D. J. Keavney, M. Vasilakaki, K. N. Trohidou, J. Sort, F. Peiró, S. Suriñach, M. D. Baró and J. Nogués, *Nanoscale*, 2012, **4**, 5138–5147.

32 D. Suess, *Appl. Phys. Lett.*, 2006, **89**, 113105.
33 M. Knobel, W. C. Nunes, L. M. Socolovsky, E. De Biasi, J. M. Vargas and J. C. Denardin, *J. Nanosci. Nanotechnol.*, 2008, **8**, 2836–2857.
34 J. Nogués and I. K. Schuller, *J. Magn. Magn. Mater.*, 1999, **192**, 203–232.
35 J. Nogués, J. Sort, V. Langlais, V. Skumryev, S. Suriñach, J. S. Muñoz and M. D. Baró, *Phys. Rep.*, 2005, **422**, 65–117.
36 J. Nogués, J. Sort, V. Langlais, S. Doppiu, B. Dieny, J. S. Muñoz, S. Suriñach and M. D. Baró, *Int. J. Nanotechnol.*, 2005, **2**, 23–42.
37 J. R. Morales, S. Tanju, W. P. Beyermann and J. E. Garay, *Appl. Phys. Lett.*, 2010, **96**, 013102.
38 J. Sort, V. Langlais, S. Doppiu, B. Dieny, J. S. Muñoz, S. Suriñach, M. D. Baró, Ch. Laurent and J. Nogués, *Nanotechnology*, 2004, **15**, S211–S214.
39 S. R. Mishra, I. Dubenko, J. Griffis, N. Ali and K. Marasinghe, *J. Alloys Compd.*, 2009, **485**, 667–671.
40 K. W. Lin, F. T. Lin, Y. M. Tzeng and Z. Y. Guo, *Eur. Phys. J. B*, 2005, **45**, 237–242.
41 N. Domingo, A. M. Testa, D. Fiorani, C. Binns, S. Baker and J. Tejada, *J. Magn. Magn. Mater.*, 2007, **316**, 155–158.
42 L. Del Bianco, D. Fiorani, A. M. Testa, E. Bonetti and L. Signorini, *Phys. Rev. B: Condens. Matter Mater. Phys.*, 2004, **70**, 052401.
43 J. Nogués, D. Lederman, T. J. Moran and I. K. Schuller, *Phys. Rev. Lett.*, 1996, **76**, 4624.